Dirac and Weyl rings in three-dimensional cold-atom optical lattices

Yong Xu[1,2] and Chuanwei Zhang[1,*]
[1]*Department of Physics, University of Texas at Dallas, Richardson, Texas 75080, USA*
[2]*Department of Physics, University of Michigan, Ann Arbor, Michigan 48109, USA*
(Received 15 November 2015; revised manuscript received 6 May 2016; published 7 June 2016)

Recently three-dimensional topological quantum materials with gapless energy spectra have attracted considerable interest in many branches of physics. Besides the celebrated example, Dirac and Weyl points which possess gapless point structures in the underlying energy dispersion, the topologically protected gapless spectrum, can also occur along a ring, named Dirac and Weyl nodal rings. Ultracold atomic gases provide an ideal platform for exploring new topological materials with designed symmetries and dispersion. However, whether Dirac and Weyl rings can exist in the single-particle spectrum of cold atoms remains elusive. Here we propose a realistic model for realizing Dirac and Weyl rings in the single-particle band dispersion of a cold-atom optical lattice. Our scheme is based on a previously experimentally implemented Raman coupling setup for realizing spin-orbit coupling. Without the Zeeman field, the model preserves both pseudo-time-reversal and inversion symmetries, allowing Dirac rings. The Dirac rings split into Weyl rings with a Zeeman field that breaks the pseudo-time-reversal symmetry. We examine the superfluidity of attractive Fermi gases in this model and also find Dirac and Weyl rings in the quasiparticle spectrum.

DOI: 10.1103/PhysRevA.93.063606

I. INTRODUCTION

The topology of band structures plays a crucial role in many important phenomena [1–4] in various physical fields. Remarkably, apart from gapped topological insulators that exhibit metallic edge states protected by symmetries [3,4], materials with gapless band dispersions could also possess nontrivial topological properties and protected edge states. A well-known example of two-dimensional gapless materials is graphene with Dirac points [2]. In recent years, gapless Dirac and Weyl points in three dimensions (3D) have been theoretically predicted [5–12] and experimentally observed [13–18] in a variety of Dirac and Weyl semimetals. Besides isolated topological gapless points, the gaps of energy spectra in 3D could also close along a line, forming Dirac and Weyl nodal rings in nodal semimetals [19–28]. However, the band dispersion of such nodal semimetals usually also consists of trivial bulk spectra at the same energy as the nodal rings, which dominate the properties of the materials over nodal rings.

Cold atomic gases provide a clean platform for discovering new topological quantum materials due to their high controllability for engineering Hamiltonians with desired symmetries and dispersion and are versatile tools for directly probing topological states. In this context, recent experimental achievements for realizing cold-atom topological matter, both gapped and gapless, mainly focus on low-dimensional (2D or 1D) systems [29–35]. In 3D, although various topological gapless structures such as traditional and structured Weyl points and rings have been theoretically predicted in quasiparticle spectra of superfluids [36–44], their realization requires very low temperature, which is unachievable within current experimental technology [45,46]. In contrast, the single-particle spectra of ultracold fermionic gases have been routinely observed in experiments at degenerate Fermi temperature [45,46]. However, apart from Weyl points [47,48], a realistic scheme for realizing Dirac and Weyl rings in single-particle spectra of cold atoms is still lacking.

In this paper, we propose an experimental scheme for engineering a Hamiltonian that hosts Dirac or Weyl rings in its single-particle spectrum of cold atoms without involving other topological trivial bulk spectra. The scheme is based on the experimentally implemented Raman coupling setup for spin-orbit coupling [45,46,49–53], and therefore it should be experimentally feasible and may pave the way for the experimental generation and observation of topological gapless materials. Our main results are the following:

(i) We construct a spin-dependent Hamiltonian in continuous space and derive its tight-binding form. Such a Hamiltonian has not been discussed previously in solid-state materials [19–27]. The Hamiltonian preserves both pseudo-time-reversal and inversion symmetries without Zeeman fields, allowing the existence of Dirac rings. The pseudo-time-reversal symmetry is broken with a Zeeman field, and a Dirac ring splits into two Weyl rings. The parameter regions as well as the topological characterization (e.g., topological invariance, surface states) for these topological gapless rings are obtained.

(ii) We investigate the superfluidity of attractive Fermi gases in this Hamiltonian and find two distinct superfluid phases. The transition between them is the first order. Interestingly, Dirac and Weyl rings also exist in quasiparticle spectra in certain superfluid regions.

(iii) The spin-dependent Hamiltonian can be realized using an experimental setup based on a previous Raman coupling scheme for spin-orbit coupling [45,46,49–53]. Specifically, two pairs of Raman laser beams are used to couple two hyperfine spin states of atoms for generating a specific spin-dependent optical lattice, which is essential for the creation of these topological nodal rings. Compared to solid-state materials, the chemical potential of the cold atomic gases can be readily tuned to the nodal rings by controlling the atom number.

*chuanwei.zhang@utdallas.edu

II. MODEL HAMILTONIAN

We start from a spin-dependent Hamiltonian in continuous space that can support the existence of nodal rings

$$H = \frac{\mathbf{p}^2}{2m} - \sum_{v=x,y,z} V_v \cos^2(k_{Lv} r_v) + h_z \sigma_z - V_{SO}\sigma_y, \quad (1)$$

where $\mathbf{p} = -i\hbar\nabla$ is the momentum operator, m is the mass of atoms, V_v and $a_v = \pi/k_{Lv}$ are respectively the strength and period of a periodic lattice along the v direction, h_z is the Zeeman field, σ_v are Pauli matrices for spins, and $V_{SO} = \Omega_{SO}\sin(k_{Lx}r_x)\cos(k_{Ly}r_y)\cos(k_{Lz}r_z)$ corresponds to a spin-dependent optical lattice. For simplicity, we explore the physics of this Hamiltonian in the tight-binding model (see the Appendix A) that can be written as

$$H_{TB} = H_h + H_Z + H_{SO}, \quad (2)$$

where $H_h = -\sum_j \sum_\sigma \sum_v (t_v \hat{c}^\dagger_{j,\sigma}\hat{c}_{j_v+1,\sigma} + t_{Nv}\hat{c}^\dagger_{j,\sigma}\hat{c}_{j_v+2,\sigma} +$ H.c.) includes the nearest-neighbor (NN) and next nearest-neighbor (NNN) hopping with the tunneling amplitudes t_v and t_{Nv}, respectively, $H_Z = h_z \sum_j (\hat{c}^\dagger_{j,\uparrow}\hat{c}_{j,\uparrow} - \hat{c}^\dagger_{j,\downarrow}\hat{c}_{j,\downarrow})$ is the Zeeman field term, and $H_{SO} = it_{\rm SO}\sum_j (-1)^{j_x+j_y+j_z}(\hat{c}^\dagger_{j,\uparrow}\hat{c}_{j_x+1,\downarrow} - \hat{c}^\dagger_{j,\uparrow}\hat{c}_{j_x-1,\downarrow}) +$ H.c. is the position-dependent spin-orbit coupling term. Here $\hat{c}^\dagger_{j,\sigma}$ ($\hat{c}_{j,\sigma}$) creates (annihilates) an atom at site j with spin σ.

The position dependent spin-orbit coupling of the Hamiltonian breaks the one-site translation symmetry, leading to a unit cell consisting of two sites: A and B. These new unit cells form a rock-salt crystal structure as shown in Fig. 1(a). In the new basis $\Psi(\mathbf{k})^T$ with $\Psi(\mathbf{k}) = (e^{ik_x a_x}\hat{A}_{\mathbf{k}\uparrow} \quad e^{ik_x a_x}\hat{A}_{\mathbf{k}\downarrow} \quad \hat{B}_{\mathbf{k}\uparrow} \quad \hat{B}_{\mathbf{k}\downarrow})$,

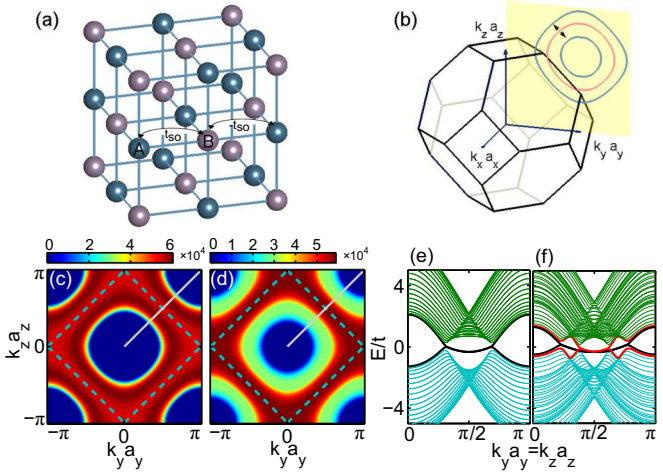

FIG. 1. (a) Rocksalt lattice structure and (b) corresponding first Brillouin zone. Dirac ($h_z = 0$) and Weyl rings ($h_z = 0.5t$), denoted by the red (central) and blue (inner and outer) rings respectively, are located at the $k_x = 0$ plane [yellow plane] around ($k_y a_y = \pi, k_z a_z = \pi$). (c) Without and (d) with h_z, density of states at zero energy without including NNN hopping when there are edges along x. The dashed square indicates the first Brillouin zone. (e), (f) Spectra along $k_y a_y = k_z a_z$ [the solid gray line in panels (c) and (d)] with edges along x with NNN hoppings, where the black and red (dark gray) lines denote the surface states. $t_x = 1.17t, t_y = t_z = t, t_{SO} = 0.53t$, and $t_N = -0.07t$. $a_x = a_y = a_z$.

the Hamiltonian in momentum space takes the form

$$H(\mathbf{k}) = h_{Nt} - h_t\tau_x + h_z\sigma_z + d_x\tau_y\sigma_y, \quad (3)$$

where $h_{Nt} = -2\sum_v t_{Nv}\cos(2k_v a_v)$, $h_t = 2\sum_v t_v \cos(k_v a_v)$, and $d_x = 2t_{SO}\sin(k_x a_x)$. τ are Pauli matrices for the A, B sublattice space. When $h_z = 0$, this Hamiltonian preserves both the pseudo-time-reversal symmetry $\mathcal{T}^{-1}H\mathcal{T} = H(-\mathbf{k})$ with $\mathcal{T} = i\tau_x\sigma_y\mathcal{K}$ [54] and $\mathcal{K}$ being the complex conjugate operator, and the inversion symmetry $\mathcal{I}^{-1}H\mathcal{I} = H(-\mathbf{k})$ with $\mathcal{I} = \tau_x$. These two symmetries guarantee that the state at each $\mathbf{k}$ is at least twofold degenerate, which implies that a gapless touching point, if exists, is fourfold degenerate. Therefore a ring formed by such gapless points is a Dirac ring. When one of the symmetries is broken, for instance, h_z breaks the pseudo-time-reversal symmetry, a Dirac ring splits into two Weyl rings, as visualized in Fig. 1(b).

The emergence of Dirac and Weyl rings can be seen from the energy spectrum of $H(\mathbf{k})$: $E_\lambda = h_{Nt} \pm \sqrt{(h_z + \lambda h_t)^2 + d_x^2}$ with $\lambda = \pm$. Clearly, two bands (four bands when $h_z = 0$) touch to form nodal rings in $\mathbf{k}$ space as shown in Fig. 1(b), when $d_x = 0$ (i.e., $k_x = 0$) and $h_z + \lambda h_t = 0$, requiring $-2t_1 < h_z < 2t_2$ or $-2t_2 < h_z < 2t_1$ with $t_1 = t_y + t_z + t_x$ and $t_2 = t_y + t_z - t_x$. Specifically, when $h_z = 0$ and $t_y + t_z > t_x$, there exists a fourfold degenerate Dirac ring. With h_z, the Dirac ring splits into Weyl rings, whose number equals the number of the above conditions satisfied. Around a point on a nodal ring, the energy dispersion is linear except along the tangent direction to the ring. At the critical points (i.e., $h_z = \pm 2t_1, \pm 2t_2$), a ring shrinks to a point around which the dispersion is quadratic.

To discuss the topology of these nodal rings, we transform the tight-binding Hamiltonian (2) by $(-1)^{j_x+j_y+j_z}\hat{c}_{j,\uparrow} \to \hat{c}_{j,\uparrow}$ [55], which transforms Eq. (3) to

$$H_1(\mathbf{k}) = h_{Nt} + d_z\sigma_z - d_x\sigma_x, \quad (4)$$

with $d_z = h_t + h_z$. The eigenvalues are $E^\pm_{\mathbf{k}} = h_{Nt} \pm \sqrt{d_x^2 + d_z^2}$, where $\pm$ refers to the helicity, the eigenvalue of $H_1(\mathbf{k})/\sqrt{d_x^2 + d_z^2}$.

This transformation simplifies the lattice structure to a simple cubic and hence enlarges the Brillouin zone so that one nodal ring in the $k_x = 0$ plane is moved to the $k_x a_x = \pi$ plane. In this transformed model that possesses the chiral symmetry, i.e., $\sigma_y H(\mathbf{k})\sigma_y = -H(\mathbf{k})$ without NNN hoppings, we see that the Weyl ring can be characterized by the winding number $n_w = \pm 1$ [56] (belongs to AIII class [57]), the number of rotations that the vector $\mathbf{d} = d_z\mathbf{e}_x - d_x\mathbf{e}_y$ undergoes when it travels along a closed trajectory enclosing any gap closing point. Such nonzero n_w also amounts to the quantized Berry phase $C_1 \bmod 2\pi = \pi$, half of the solid angle that $\mathbf{d}$ winds [58]. For a Dirac ring, the Hamiltonian (3) ($h_z = 0$) respects a σ_y symmetry, i.e., $\sigma_y H(\mathbf{k})\sigma_y = H(\mathbf{k})$ and hence the classification is $\mathbb{Z} \times \mathbb{Z}$; i.e., each band in two subspaces with different eigenvalues $\sigma_y = \pm 1$ has a quantized Berry phase [59,60]. We note that although the NNN hopping breaks the chiral symmetry by changing the eigenvalues, it does not modify the eigenstates, thereby leaving the quantized Berry phase unchanged.

In Figs. 1(c) and 1(d), we plot the surface density of states at zero energy (without NNN hoppings) when the edges are

imposed along the x direction in the model (2). The density of states is extremely large between rings in different Brillouin zones, implying the vanishing dispersion of the surface states (i.e., the surface spectrum is flat). With NNN hoppings, the surface spectrum gains a slight dispersion as shown in Figs. 1(e) and 1(f), where the black and red lines denote the surface spectra. Without h_z, the surface spectra are fourfold degenerate, whereas with h_z, this fourfold degeneracy is lifted so that the surface states connecting different pairs of gapless points are separated (black and red lines). This breaking is also reflected in Fig. 1(d) where the density of states in the red region is twice as large as that in the green one.

III. SUPERFLUIDS IN NODAL RING LATTICES

The Dirac and Weyl nodal ring lattices can be realized for both Bose and Fermi atoms. Here we consider fermionic cold atoms with contact attractive interactions that can be tuned by Feshbach resonances. With attractive interactions, Fermi gases form superfluids. Under the mean-field approximation, we can define the order parameter for both A and B sublattices, respectively, as $\Delta_A = -U\langle \hat{A}_{j\downarrow}\hat{A}_{j\uparrow}\rangle$ and $\Delta_B = -U\langle \hat{B}_{j\downarrow}\hat{B}_{j\uparrow}\rangle$ with the interaction strength U ($U > 0$). Note that we only consider the case with spatially uniform Δ_A and Δ_B corresponding to the BCS pairing with zero center-of-mass momenta [61]. The dynamics of the superfluid is governed by the Bogliubov–de Gennes (BdG) Hamiltonian

$$H_{\rm BdG} = -s_z(h_t\tau_x + \tilde{\mu}) + d_x\tau_y\sigma_y + h_z\sigma_z + H_{\rm BCS}, \qquad (5)$$

where $\tilde{\mu} = \mu - h_{Nt}$ with the chemical potential μ, and Pauli matrices s act on the Nambu particle-hole space. This Hamiltonian is written in the Nambu basis $(\Psi(\mathbf{k}) \quad \tilde{\Psi}(\mathbf{k}))^T$ with $\tilde{\Psi}(\mathbf{k}) = (e^{ik_xa_x}\hat{A}^\dagger_{-\mathbf{k}\downarrow} \quad -e^{ik_xa_x}\hat{A}^\dagger_{-\mathbf{k}\uparrow} \quad \hat{B}^\dagger_{-\mathbf{k}\downarrow} \quad -\hat{B}^\dagger_{-\mathbf{k}\uparrow})$. Δ_A and Δ_B are obtained by numerically solving the nonlinear gap equations, $\partial\Omega/\partial\Delta_A = 0$ and $\partial\Omega/\partial\Delta_B = 0$, where Ω is the thermodynamical potential per site [40].

Before we show the numerical results of Δ_A and Δ_B, we first analyze the conditions under which Dirac and Weyl rings can emerge in quasiparticle spectra. Our numerical results show that real Δ_A and Δ_B with $\Delta_A = |\Delta_B|$ are energetically preferred; therefore we only need to consider two superfluids phases: $\Delta_A = \Delta_B$ (dubbed SF1) and $\Delta_A = -\Delta_B$ (dubbed SF2), associated with $H_{BCS} = \Delta_A s_x$ and $H_{BCS} = \Delta_A s_x\tau_z$, respectively. When $h_z = 0$, both phases preserve the pseudo-time-reversal and inversion symmetries [62], guaranteeing that the quasiparticle spectra are at least twofold degenerate at each $\mathbf{k}$. Therefore gapless rings, if exist, are fourfold degenerate Dirac rings because of these two symmetries and the intrinsic particle-hole symmetry. Finite h_z breaks the pseudo-time-reversal symmetry and splits the Dirac ring into two twofold degenerate Weyl rings.

Specifically, for the SF1 state, without h_z, the eigenvalues of $H_{\rm BdG}$ are $E^\lambda_{\mathbf{k}\pm} = \pm\sqrt{h_0^2 + h_t^2 + d_x^2 + 2\lambda\sqrt{\tilde{\mu}^2h_t^2 + h_0^2d_x^2}}$ with $h_0^2 = \Delta_A^2 + \tilde{\mu}^2$ and $\lambda = \pm$. Each spectrum is twofold degenerate. From $(E^+_{\mathbf{k}+})^2(E^-_{\mathbf{k}+})^2 = (h_0^2 - h_t^2 - d_x^2)^2 + 4\Delta_A^2h_t^2$, we see that $h_t = 0$ and $d_x^2 = h_0^2$ for gapless rings. The latter condition requires $\mu^2 \leqslant 4t_{SO}^2 - \Delta_A^2$, if NNN hoppings are neglected. For the SF2 state, $E^{\lambda\nu}_{\mathbf{k}\pm} = \pm\sqrt{h_0^2 + (h_z + \nu h_t)^2 + d_x^2 + 2\lambda\sqrt{h_0^2(h_z + \nu h_t)^2 + \tilde{\mu}^2d_x^2}}$ with $\nu = \pm$. When $h_z = 0$, the spectra are twofold degenerate, and this degeneracy is explicitly broken by h_z. Still, by $(E^{+\nu}_{\mathbf{k}+})^2(E^{-\nu}_{\mathbf{k}+})^2 = [-h_0^2 + (h_z + \nu h_t)^2 + d_x^2]^2 + 4\Delta_A^2d_x^2$, we see that nodal rings appear when $d_x = 0$ and $(h_z + \nu h_t)^2 = h_0^2$. This leads to the existence of rings in the $k_x = 0$ plane when $-2t_1 + h_0 < h_z < 2t_2 + h_0$ or $-2t_1 - h_0 < h_z < 2t_2 - h_0$ or $-2t_2 + h_0 < h_z < 2t_1 + h_0$ or $-2t_2 - h_0 < h_z < 2t_1 - h_0$, if NNN hoppings are not involved. For Weyl rings ($h_z \neq 0$), their number equals to the number of the above relations satisfied, which allow at most two Weyl rings when $h_0 > 2(t_y + t_z)$. We note that without h_z, the rings are Dirac rings, which split into Weyl rings when h_z is turned on. We also note that NNN hoppings only slightly modify the shape of nodal rings.

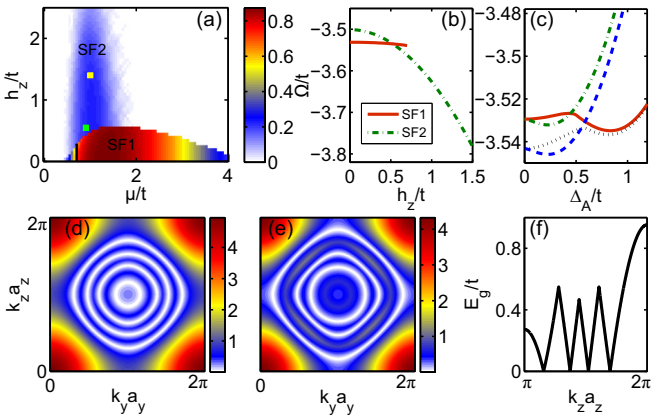

FIG. 2. (a) The order parameter Δ_A as a function of μ and h_z at zero temperature. SF1 and SF2 correspond to the phases with $\Delta_A = \Delta_B$ and $\Delta_A = -\Delta_B$, respectively. A black line divides SF1 phase into gapless (left part) and gapped (right part) regions, while the whole SF2 phase is gapless. (b) The thermodynamical potential Ω of the SF1 (solid red line) and SF2 (dotted-dashed green line) phases with respect to h_z with $\mu = 1.1t$. Note that when $h_z > 0.7t$ the SF1 state is no longer a local energy minimum state, while the SF2 state is in the whole region. (c) Ω as a function of Δ_A for SF1 (solid red and dotted black lines) and SF2 (dotted-dashed green and dashed blue lines). Solid red and dotted-dashed green lines are for $\mu = 1.1t$, $h_z = 0.5t$, and dotted black and dashed blue lines are for $\mu = 1.1t$, $h_z = 0.6t$, respectively. (d), (e) The gap E_g of quasiparticle spectra in (k_ya_y, k_za_z) with $k_x = 0$ for the parameters denoted by the green (lower) and yellow (upper) squares in panel (a), respectively. (f) The gap E_g in panel (d) along k_z for fixed $k_ya_y = \pi$. Here $t_x = 1.17t$, $t_y = t_z = t$, $t_{SO} = 0.53t$, $t_N = -0.07t$, and $U = -4t$. $a_x = a_y = a_z$.

In Fig. 2(a), we plot the order parameter Δ_A in the (μ, h_z) plane and there exist two superfluid phases: SF1 and SF2. Such two phases can be understood in two limits. In the first limit, we assume $t_{SO} = 0$ and clearly $\Delta_A = \Delta_B$ as A and B sublattices can now be connected by a translational transformation. In the second limit, we assume $t_\nu = t_{N\nu} = 0$, and in the transformed model, the momenta of Cooper pairs are zero, meaning that $\Delta_B = -\Delta_A$ in the original model. Although these two states can be simultaneously the local energy minimum states as shown in Fig. 2(c), the ground state should be the global energy minimum state (i.e., the one with the lower energy). Therefore with the change of parameters, these two phases can transition

from one to another as shown in Fig. 2(b), where the ground state changes from SF1 to SF2 with increasing h_z. Clearly, this phase transition is the first order.

By examining the quasiparticle spectrum, we find that the SF1 phase is gapless only in a small region (the left part of the black line), whereas the SF2 phase is gapless in the whole region. In Figs. 2(d) and 2(e), we plot the gap (i.e., $E_g = \min(|E_{\mathbf{k}\gamma}|)$) of the quasiparticle spectrum in the $k_x = 0$ plane for the parameters associated with the green and yellow squares in Fig. 2(a), displaying four and three Weyl rings, respectively. The gap along k_z for fixed $k_y a_y = \pi$ for the former is plotted in Fig. 2(f). Similar to the nodal rings in single-particle spectra, the number of rings can be tuned by Zeeman fields or chemical potential. Such Weyl rings can also be characterized by the winding number $n_w = \pm 1$ (see the Appendix B). For Dirac rings in the SF1 phase when $h_z = 0$, they can be characterized by the winding number in two subspaces with different eigenvalues $\sigma_y = \pm 1$.

IV. REALIZATION OF NODAL RING LATTICES

We propose an experimental setup (shown in Fig. 3) based on Raman coupling scheme for generating spin-orbit coupling [35,45,46,49–53] to engineer the Hamiltonian (1).

Two independent pairs of red-detuned Raman lasers are used to couple two hyperfine states (see the Appendix A for experimental parameters). One pair corresponds to the lasers Ω_1 and Ω_2 with the Rabi frequencies $\Omega_1 = \Omega_{10}\cos(k_{Ry}r_y)e^{-ik_{Rz}r_z/2}$ and $\Omega_2 = i\Omega_{20}\sin(k_{Rx}r_x)e^{ik_{Rz}r_z/2}$, each of which can be generated by two plane wave lasers. The other pair of Raman lasers have the Rabi frequencies $\Omega_1' = \Omega_{10}'\cos(k_{Ry}r_y)e^{ik_{Rz}r_z/2}$ and $\Omega_2' = i\Omega_{20}'\sin(k_{Rx}r_x)e^{-ik_{Rz}r_z/2}$, respectively. Such two sets of Raman lasers give rise to the spin-dependent lattice with $\Omega_{SO} = 2\Omega$ and $k_{Lv} = k_{Rv}$ in Eq. (1) when $\Omega = \Omega'$, achieved when the two sets of Raman lasers come from the same resource. These lasers also lead to the optical lattices along the x and y directions via the Stark effects: $-\delta V_x \sin^2(k_{Rx}r_x)$ and $-V_y\cos^2(k_{Ry}r_y)$ with $\delta V_x = (|\Omega_{20}|^2 + |\Omega_{20}'|^2)/\Delta_e$ and $V_y = (|\Omega_{10}|^2 + |\Omega_{10}'|^2)/\Delta_e$. Moreover, one needs another stronger optical lattices along the x direction: $-V_x'\cos^2(k_{Rx}r_x)$ with $V_x' > 0$ so that the total x direction optical lattice is $-V_x\cos^2(k_{Rx}r_x)$ with $V_x = V_x' - \delta V_x > 0$. Similarly, the optical lattices along z, $-V_z\cos^2(k_{Rz}r_z)$ with $V_z > 0$, can be generated. We note that the Raman lasers can also create the Zeeman field $h_z = \delta/2$ with δ being the two-photon detuning.

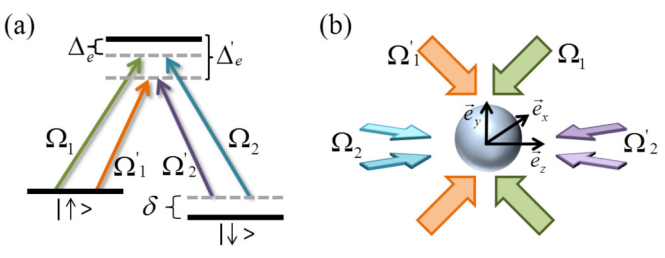

FIG. 3. Schematics of a laser configuration to realize the Hamiltonian (1). Ω_1 and Ω_2, Ω_1' and Ω_2' are two sets of Raman laser beams coupling two hyperfine states $|\uparrow\rangle$ and $|\downarrow\rangle$. Δ_e and Δ_e' are the detunings, and δ is the two-photon detuning. Each Raman laser beam consists of two plane wave laser beams as shown in panel (b). These Raman laser beams also generate optical lattices via the Stark effects. Additional laser beams are also employed to create optical lattices along x and z.

To detect the Dirac and Weyl rings in the single-particle and quasiparticle spectrum [37,44] of Fermi atoms, one can consider the momentum-resolved radio-frequency spectroscopy, similar to that in spin-orbit-coupled atomic gases [35,45,46] and conventional superfluids [63]. In terms of a BEC loaded in nodal ring lattices, one can measure Landau-Zener tunneling probability to detect the rings [34,48] and the interference between two BECs traveling across a Weyl ring to extract the Berry phase [64].

V. DIRAC CONES IN TWO DIMENSIONS

Not only nodal rings in 3D can be realized in the proposed experimental setup, but also Dirac cones in 2D can be engineered in a much simpler setup as shown in Figs. 4(a) and 4(b), where only a pair of Raman laser beams with Rabi frequencies $\Omega_1 = \Omega_{10}\cos(k_R y)$ and $\Omega_2 = i\Omega_{20}\sin(k_R x)$ is required, and an additional standing laser beam is used to engineer an optical lattice along x. This laser setup leads to the following Hamiltonian:

$$H_{2D} = \frac{\mathbf{p}^2}{2m} - \sum_{v=x,y} V_v\cos^2(k_R r_v) + h_z\sigma_z - V_{SO}\sigma_y, \qquad (6)$$

where $V_{SO} = \Omega_{SO}\sin(k_{L_R}r_x)\cos(k_{L_R}r_y)$. The tight-binding model of this Hamiltonian is a simplified version of Eq. (2) when the hopping terms along x and y are kept and

$$H_{SO} = it_{\mathrm{SO}}\sum_j (-1)^{j_x+j_y}(\hat{c}^\dagger_{j,\uparrow}\hat{c}_{j_x+1,\downarrow} - \hat{c}^\dagger_{j,\uparrow}\hat{c}_{j_x-1,\downarrow}) + \mathrm{H.c.} \qquad (7)$$

Clearly, the Hamiltonian in momentum space is also a simplified version of the Hamiltonian (3) in the main text when only the hopping terms along x and y are kept. In contrast to 2D Dirac cones in honeycomb lattices in previous experiments [34], there are two types of Dirac cones appearing when $h_z + \lambda h_t = 0$ on the $k_x = 0$ line: one with fourfold degeneracies (each with Berry phase being π or $-\pi$ in the subspaces with $\sigma_y = \pm 1$ similar to the 3D case) and one with twofold degeneracies (each with Berry phase being π or $-\pi$). Without Zeeman fields, the former can exist [as displayed in Fig. 4(c)] only when $t_y > t_x$, which can be realized by choosing a stronger optical lattice along the x direction than that along the y direction. At the critical point $t_y = t_x$, the spectrum becomes quadratic along y and keeps linear along x. In the presence of h_z, each Dirac cone with fourfold degeneracies splits into two Dirac cones with twofold degeneracies in separated positions in momentum space as shown in Fig. 4(d). They can exist as long as $2(t_x - t_y) < h_z < 2(t_y + t_x)$ and $-(t_x + t_y) < h_z < 2(t_y - t_x)$. When $h_z = \pm 2(t_x + t_y)$ and $h_z = \pm 2(t_y - t_x)$, two Dirac cones with twofold degeneracies merge—with spectra being quadratic along y and linear along x—at $(k_x = 0, k_y = 0)$ and $(k_x = 0, k_y = \pi)$, respectively. Evidently, such Dirac cones can be readily created, moved, and merged by tuning the lattice strength and Zeeman fields. Note that in previous experiments [34], the Dirac cones are formed due to the

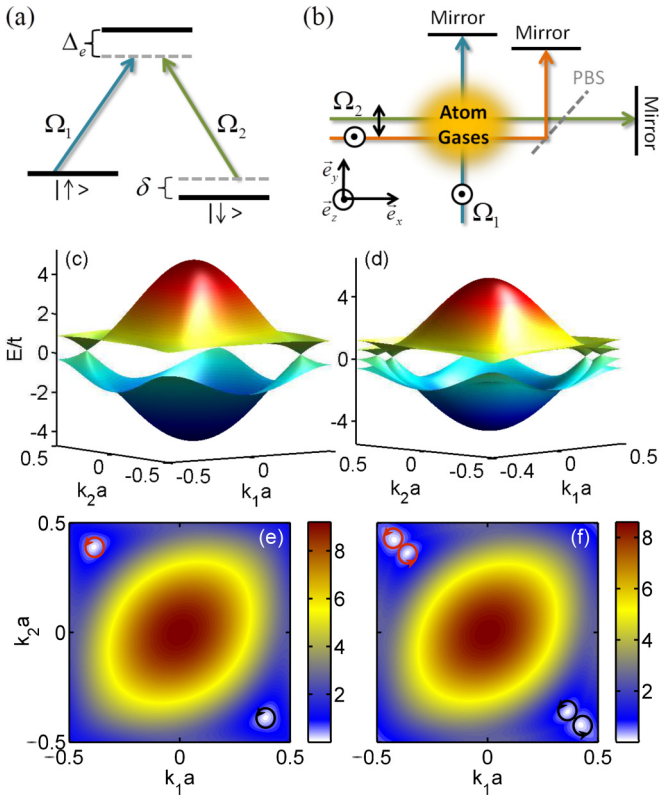

FIG. 4. (a), (b) Schematics of a laser configuration to realize the 2D Hamiltonian with Dirac cones and the single-particle spectra of such optical lattice systems. Ω_1 and Ω_2 are two Raman laser beams coupling two hyperfine states $|\uparrow\rangle$ and $|\downarrow\rangle$. Δ_e is the detuning, and δ is the two-photon detuning. Each Raman laser beam is a standing wave formed by a plane wave laser beam reflected by a mirror as shown in panel (b). These Raman laser beams also generate optical lattices via the Stark effects. An additional laser beam (red line) with different frequency from the Raman lasers (shifted by $\sim$100 MHz using an acoustic-optical modulator, AOM) is also employed to create optical lattices along x. PBS denotes polarizing beam splitter. Double arrows and circle dots denote the polarization direction of laser beams. The PBS separates the Raman beam and the optical lattice beams so that their phases can be controlled individually by different mirrors. (c), (d) Single-particle spectra of the tight-binding Hamiltonian without and with Zeeman fields, respectively. (e), (f) The gap distribution between particle and hole branches in momentum space. The white points indicate the Dirac cones and the Berry phase calculated along the red (top left) circle [black (bottom right) one] is π ($-\pi$). Note in panel (e) the Berry phase is calculated in the subspace of σ_y. Here $t_x = t$, $t_y = 1.3t$, $t_N = 0.07t$, and $t_{SO} = 0.64t$. The lattice constants are $a_x = a_y = a$ and the crystal momenta are $a\mathbf{k} = \pi(k_1 + k_2)\mathbf{e}_x + \pi(-k_1 + k_2)\mathbf{e}_y$.

honeycomb lattice structure and the spin Zeeman field only shifts the relative energy between two Dirac cones for different spins, not their positions in momentum space. In our model, the Zeeman field can split a fourfold degenerate Dirac cone into two located at different positions in momentum space.

ACKNOWLEDGMENTS

We would like to thank P. Engels, F. Zhang, and C. Liu for helpful discussions. This work is supported by ARO (W911NF-12-1-0334), AFOSR (FA9550-13-1-0045), and NSF (PHY-1505496). We also thank Texas Advanced Computing Center, where part of our numerical calculations was performed.

APPENDIX A: DERIVATION OF TIGHT-BINDING MODEL

In this appendix, we derive the tight-binding model from the continuous model (1) in the main text and compare the single-particle spectra of the tight-binding and continuous models for typical parameters in experiments.

In the second quantization representation, the Hamiltonian takes the form

$$H_{II} = \int d\mathbf{r}\hat{\psi}^\dagger(\mathbf{r})H\hat{\psi}(\mathbf{r}), \tag{A1}$$

where H is the single-particle Hamiltonian in Eq. (1) in the main text, $\hat{\psi}(\mathbf{r}) = (\hat{\psi}_\uparrow(\mathbf{r}) \quad \hat{\psi}_\downarrow(\mathbf{r}))^T$, where $\hat{\psi}_\sigma(\mathbf{r})$ [$\hat{\psi}^\dagger_\sigma(\mathbf{r})$] annihilates (creates) an atom with spin σ ($\sigma = \uparrow, \downarrow$) located at $\mathbf{r}$. They satisfy the anticommutation or commutation relation $[\hat{\psi}_\sigma(\mathbf{r}), \hat{\psi}^\dagger_{\sigma'}(\mathbf{r}')]_\pm = \delta_{\sigma\sigma'}\delta(\mathbf{r} - \mathbf{r}')$ for fermionic atoms (+) or bosonic atoms (−), respectively. The field operator can be expanded by local Wannier functions

$$\hat{\psi}_\sigma(\mathbf{r}) = \sum_{nj\sigma} W_{nj\sigma}\hat{c}_{n,j,\sigma}, \tag{A2}$$

where $W_{nj\sigma}$ is the Wannier function located at the jth site for the nth band for spin σ, and $\hat{c}_{n,j,\sigma}$ annihilates an atom at the jth site in the nth band with spin σ. As we only consider the physics in the lowest band, let us assume $n = 1$ and further assume that the Wannier function $W_{1j\sigma}$ can be approximated by the lowest band Wannier function W_j of the Hamiltonian with pure spin-independent optical lattices. Hence

$$\hat{\psi}_\sigma(\mathbf{r}) \approx \sum_j W_j\hat{c}_{j,\sigma}, \tag{A3}$$

where $W_j = W^x_{j_x}(r_x)W^y_{j_y}(r_y)W^z_{j_z}(r_z)$ with $W^\nu_{j_\nu}(r_\nu) = W^\nu(r_\nu - j_\nu a_\nu)$ being the Wannier function along ν. Based on this expansion, the tight-binding model without H_{SO} reads

$$H_1 = -\sum_j\sum_\sigma\sum_\nu \left(t_\nu\hat{c}^\dagger_{j,\sigma}\hat{c}_{j_\nu+1,\sigma} + t_{N\nu}\hat{c}^\dagger_{j,\sigma}\hat{c}_{j_\nu+2,\sigma} + \text{H.c.}\right) + h_z\sum_j(\hat{c}^\dagger_{j,\uparrow}\hat{c}_{j,\uparrow} - \hat{c}^\dagger_{j,\downarrow}\hat{c}_{j,\downarrow}) \tag{A4}$$

with the inclusion of the nearest and next nearest neighbor hopping with the corresponding hopping amplitudes being

$$t_\nu = -\int dr_\nu W_j\left[\frac{p_\nu^2}{2m} - V_\nu\cos^2(k_{L\nu}r_\nu)\right]W_{j_\nu+1}, \tag{A5}$$

$$t_{N\nu} = -\int dr_\nu W_j\left[\frac{p_\nu^2}{2m} - V_\nu\cos^2(k_{L\nu}r_\nu)\right]W_{j_\nu+2}. \tag{A6}$$

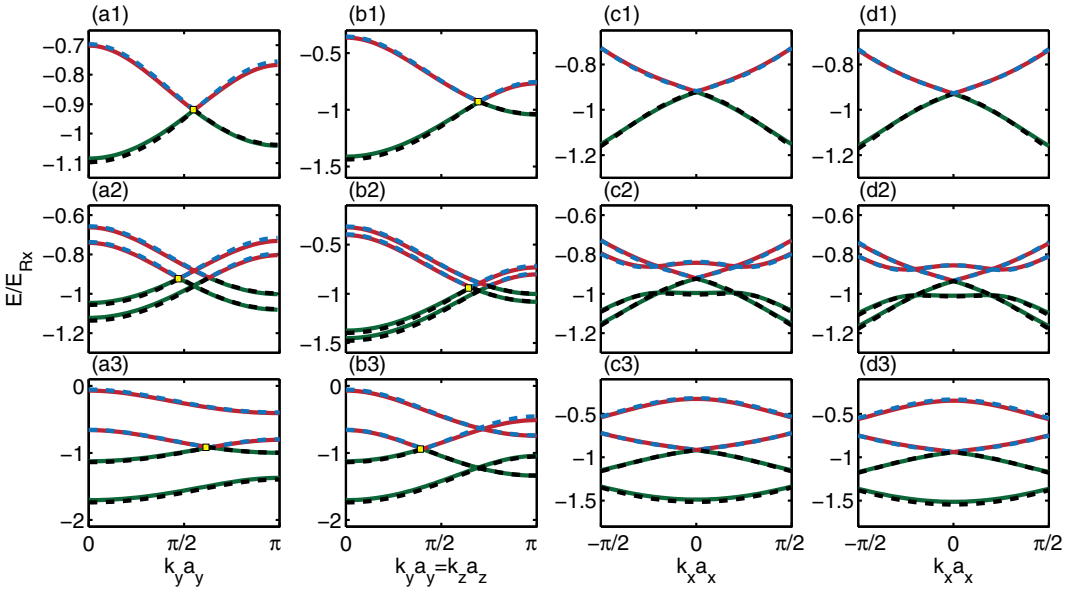

FIG. 5. Single-particle spectra obtained by the tight-binding model [dashed blue (upper) and black (lower) lines] and the continuous model [solid red (upper) and green (lower) lines]. Each row panel from top to bottom is associated with $h_z = 0$, $h_z = 0.032E_R$, and $h_z = 0.24E_R$, respectively. The first and second column panels (from left to right) correspond to ($k_x = 0, k_z a_z = \pi$) and ($k_x = 0$), respectively. The third and fourth column panels plot the spectra along k_x around touching points [yellow squares] corresponding to the first and second column panels, respectively. The parameters for the continuous model are $k_{Lx} = k_{Ly} = k_{Lz} = \sqrt{4/5}k_R$, $V_x = V_y = V_z = 3.2E_R$, and $\Omega_{SO} = 0.8E_R$; the parameters for the tight-binding model are $t = t_y = t_z = 0.068E_R$ and $t_N = -0.07t$ and $t_{SO} = 0.53t$. The recoil energy along x is $E_{Rx} = \hbar^2 k_{Lx}^2/2m = 0.8E_R$.

The tight-binding term contributed by the spin-dependent lattices can be derived as follows:

$$H_{SO} = i\Omega_{SO}\int d\mathbf{r}\hat{\psi}_\uparrow^\dagger(\mathbf{r})V_{SO}\hat{\psi}_\downarrow(\mathbf{r}) + \text{H.c.} \tag{A7}$$

$$\approx i\Omega_{SO}\sum_{j,j'}\hat{c}_{j,\uparrow}^\dagger\hat{c}_{j',\downarrow}t_{SO}^{jj'} + \text{H.c.}, \tag{A8}$$

where

$$t_{SO}^{jj'} = \int d\mathbf{r}W_j V_{SO} W_{j'} = \prod_{v=x,y,z} t_{SO}^{j_v j'_v}, \tag{A9}$$

with

$$t_{SO}^{j_x j'_x} = t_{SO}^{j'_x j_x} = \int dr_x W_{j_x}^x(r_x)\sin(k_{Lx}r_x)W_{j'_x}^x(r_x), \tag{A10}$$

$$t_{SO}^{j_y j'_y} = t_{SO}^{j'_y j_y} = \int dr_y W_{j_y}^y(r_y)\cos(k_{Ly}r_y)W_{j'_y}^y(r_y), \tag{A11}$$

$$t_{SO}^{j_z j'_z} = t_{SO}^{j'_z j_z} = \int dr_z W_{j_z}^z(r_z)\cos(k_{Lz}r_z)W_{j'_z}^z(r_z). \tag{A12}$$

Because one of the optical wells is located at $\mathbf{r} = (0,0,0)$, $W_0^v(r_v) = W_0^v(-r_v)$ and

$$t_{SO}^{j_x j_x} = t_{SO}^{j_x j_x+2} = t_{SO}^{j_y j_y+1} = t_{SO}^{j_z j_z+1} = 0, \tag{A13}$$

$$t_{SO}^{j_v j_v+1} = -t_{SO}^{j_v+1 j_v+2}, \tag{A14}$$

$$t_{SO}^{j_v j_v} = -t_{SO}^{j_v+1 j_v+1}, \tag{A15}$$

where the last two relations are obtained because the period of the spin-independent optical lattices is a half of that of the spin-dependent ones along each direction. Therefore, with the nearest-neighbor hopping (no next nearest-neighbor hopping exists), the position-dependent spin-orbit coupling term of the tight-binding model reads

$$H_{SO} = i\Omega_{SO}\sum_j\left[\hat{c}_{j,\uparrow}^\dagger\hat{c}_{j_x+1,\downarrow}t_{SO}^{j_x j_x+1}t_{SO}^{j_y j_y}t_{SO}^{j_z j_z}\right.$$

$$\left. + \hat{c}_{j,\uparrow}^\dagger\hat{c}_{j_x-1,\downarrow}t_{SO}^{j_x j_x-1}t_{SO}^{j_y j_y}t_{SO}^{j_z j_z}\right] + \text{H.c.} \tag{A16}$$

$$= i\Omega_{SO}\sum_j\left[\hat{c}_{j,\uparrow}^\dagger\hat{c}_{j_x+1,\downarrow} - \hat{c}_{j,\uparrow}^\dagger\hat{c}_{j_x-1,\downarrow}\right]$$

$$\times t_{SO}^{j_x j_x+1}t_{SO}^{j_y j_y}t_{SO}^{j_z j_z} + \text{H.c.} \tag{A17}$$

$$= it_{SO}\sum_j(-1)^{j_x+j_y+j_z}\left[\hat{c}_{j,\uparrow}^\dagger\hat{c}_{j_x+1,\downarrow} - \hat{c}_{j,\uparrow}^\dagger\hat{c}_{j_x-1,\downarrow}\right] + \text{H.c.}, \tag{A18}$$

where

$$t_{SO} = \Omega_{SO}t_{SO}^{01}t_{SO}^{00}t_{SO}^{00}. \tag{A19}$$

Therefore, we obtain the tight-binding model in Eq. (2) in the main text ($H_1 = H_h + H_Z$).

In experiments, we consider ^{40}K atoms and choose $\Delta_e = 2\pi\times 1.46$ THz that can be realized by a red-detuned laser beam with wavelength 773 nm [45], which gives the recoil energy $E_R/\hbar = 2\pi\times 8.3$ kHz. A simple geometry of laser beams gives rise to $k_{Rx} = k_{Ry} = k_{Rz} = \sqrt{4/5}k_R$. The two pairs of Raman laser beams are independent as $|\Delta_e - \Delta'_e| \sim 2\pi\times(10-100)$ MHz $\gg E_R$. For $\Omega_{10} = \Omega'_{10} = 2\pi\times 0.14$ GHz and $\Omega_{20} = \Omega'_{20} = 2\pi\times 0.035$ GHz, we have $\Omega_{SO} = 0.8E_R$, $V_y = 3.2E_R$, and $\delta V_x = V_y/16$. For $\Omega_{3x} = \Omega_{3z} = 2\pi\times 0.21$ GHz, we have

$V_x' = V_z = V_y$. δ can be readily tuned from zero. With these experimental parameters, the tight-binding parameters are calculated from Eqs. (A5), (A6), and (A19), yielding $t = t_y = t_z = 0.068E_R$, $t_{Nv} = t_N = -0.07t$, and $t_{SO} = 0.53t$. We note that we choose $t_x = 1.17t$, which is slightly different from t_y and t_z given the distinct correction of Wannier functions by V_{SO} along x. We also note that we neglect the next-to-next-nearest-neighbor hoppings such as $\hat{c}^\dagger_{j,\uparrow}\hat{c}_{j_x+1,j_y+2,\downarrow}$ because of their very small effects (about $0.0034t$). Although we choose the Wannier functions for $V_{SO} = h_z = 0$ [so that $W_0^v(r_v) = W_0^v(-r_v)$] as the basis to obtain the tight-binding model, we have verified its reliability by comparing its single-particle spectra with that obtained by the continuous model in Fig. 5, which shows their good agreement with each other. However, when $\Omega_{SO} > 1.9E_R$ (much larger than $\Omega_{SO} = 0.8E_R$ used in the paper), the spectra obtained by the continuous model fail to show the nodal rings, suggesting that the tight-binding model cannot faithfully characterize the original continuous model.

APPENDIX B: WINDING NUMBER CHARACTERIZING DIRAC AND WEYL RINGS IN SUPERFLUIDS

In this section, we define the winding number for superfluids. Both SF1 and SF2 phases have the chiral symmetry (i.e., $\mathcal{C}^{-1}H_{BdG}\mathcal{C} = -H_{BdG}$ with $\mathcal{C} = \sigma_x s_y$), and we can define a winding number n_w along any 1D closed path enclosing a Weyl ring [56] belonging to the AIII class [57],

$$n_w = \frac{1}{2\pi i}\int_{\theta=-\pi}^{\theta=\pi} d\theta \frac{d}{d\theta}\log\det A(\theta), \tag{B1}$$

where $A(\theta) = H_0 + i\Delta_A\sigma_y$ for the SF1 phase and $A(\theta) = H_0 - i\Delta_A\tau_y\sigma_y$ for the SF2 phase, with $H_0 = -(h_t\tau_x + \tilde{\mu}) + d_x\tau_z\sigma_x + h_z\sigma_z$ and $k_v = k_v(\theta)$ referring to a 1D closed path. We find $n_w = \pm 1$ for Weyl rings and the associated Berry phase is $\pm\pi$. In the SF1 phase, when $h_z = 0$, there exist Dirac rings and the classification is $\mathbb{Z}\times\mathbb{Z}$, which can be characterized by the winding number in the two subspaces with different eigenvalues $\sigma_y = \pm 1$.

[1] G. E. Volovik, *The Universe in a Helium Droplet* (Clarendon Press, Oxford, UK, 2003).

[2] A. H. Castro Neto, F. Guinea, N. M. R. Peres, K. S. Novoselov, and A. K. Geim, The electronic properties of graphene, Rev. Mod. Phys. **81**, 109 (2009).

[3] M. Z. Hasan and C. L. Kane, Topological insulators, Rev. Mod. Phys. **82**, 3045 (2010).

[4] X.-L. Qi and S.-C. Zhang, Topological insulators and superconductors, Rev. Mod. Phys. **83**, 1057 (2011).

[5] S. M. Young, S. Zaheer, J. C. Y. Teo, C. L. Kane, E. J. Mele, and A. M. Rappe, Dirac Semimetal in Three Dimensions, Phys. Rev. Lett. **108**, 140405 (2012).

[6] X. Wan, A. M. Turner, A. Vishwanath, and S. Y. Savrasov, Topological semimetal and Fermi-arc surface states in the electronic structure of pyrochlore iridates, Phys. Rev. B **83**, 205101 (2011).

[7] K.-Y. Yang, Y.-M. Lu, and Y. Ran, Quantum Hall effects in a Weyl semimetal: Possible application in pyrochlore iridates, Phys. Rev. B **84**, 075129 (2011).

[8] A. A. Burkov and L. Balents, Weyl Semimetal in a Topological Insulator Multilayer, Phys. Rev. Lett. **107**, 127205 (2011).

[9] G. Xu, H. Weng, Z. Wang, X. Dai, and Z. Fang, Chern Semimetal and the Quantized Anomalous Hall Effect in $HgCr_2Se_4$, Phys. Rev. Lett. **107**, 186806 (2011).

[10] L. Lu, L. Fu, J. D. Joannopoulos, and M. Soljačić, Weyl points and line nodes in gapless gyroid photonic crystals, Nat. Photon. **7**, 294 (2013).

[11] H. Weng, C. Fang, Z. Fang, B. A. Bernevig, and X. Dai, Weyl Semimetal Phase in Noncentrosymmetric Transition-Metal Monophosphides, Phys. Rev. X **5**, 011029 (2015).

[12] S.-M. Huang *et al.*, A Weyl Fermion semimetal with surface Fermi arcs in the transition metal monopnictide TaAs class, Nat. Commun. **6**, 7373 (2015).

[13] M. Neupane *et al.*, Observation of a three-dimensional topological Dirac semimetal phase in high-mobility Cd_3As_2, Nat. Commun. **5**, 3786 (2014).

[14] S. Borisenko, Q. Gibson, D. Evtushinsky, V. Zabolotnyy, B. Buchner, and R. J. Cava, Experimental Realization of a Three-Dimensional Dirac Semimetal, Phys. Rev. Lett. **113**, 027603 (2014).

[15] Z. K. Liu *et al.*, Discovery of a three-dimensional topological Dirac semimetal, Na_3Bi, Science **343**, 864 (2014).

[16] L. Lu, Z. Wang, D. Ye, L. Ran, L. Fu, J. D. Joannopoulos, and M. Soljačić, Experimental observation of Weyl points, Science **349**, 622 (2015).

[17] X.-Y. Xu *et al.*, Experimental realization of a topological Weyl semimetal phase with Fermi arc surface states in TaAs, Science **349**, 613 (2015).

[18] B. Q. Lv, H. M. Weng, B. B. Fu, X. P. Wang, H. Miao, J. Ma, P. Richard, X. C. Huang, L. X. Zhao, G. F. Chen, Z. Fang, X. Dai, T. Qian, and H. Ding, Experimental Discovery of Weyl Semimetal TaAs, Phys. Rev. X **5**, 031013 (2015).

[19] A. A. Burkov, M. D. Hook, and L. Balents, Topological nodal semimetals, Phys. Rev. B **84**, 235126 (2011).

[20] J.-M. Carter, V. V. Shankar, M. A. Zeb, and H.-Y. Kee, Semimetal and topological insulator in perovskite iridates, Phys. Rev. B **85**, 115105 (2012).

[21] Y. Chen, Y.-M. Lu, and H.-Y. Kee, Topological crystalline metal in orthorhombic perovskite iridates, Nat. Commun. **6**, 6593 (2015).

[22] R. Schaer, E. K. H. Lee, Y.-M. Lu, and Y. B. Kim, Topological Spinon Semimetals and Gapless Boundary States in Three Dimensions, Phys. Rev. Lett. **114**, 116803 (2015).

[23] Y. Chen, Y. Xie, S. A. Yang, H. Pan, F. Zhang, M. L. Cohen, and S. Zhang, Spin-orbit-free Weyl-loop and Weyl-point semimetals in a stable three-dimensional carbon allotrope, Nano Lett. **15**, 6974 (2015).

[24] Y. Kim, B. J. Wieder, C. L. Kane, and A. M. Rappe, Dirac Line Nodes in Inversion Symmetric Crystals, Phys. Rev. Lett. **115**, 036806 (2015).

[25] L. S. Xie, L. M. Schoop, E. M. Seibel, Q. D. Gibson, W. Xie, and R. J. Cava, Potential ring of Dirac nodes in a new polymorph of Ca_3P_2, APL Mater. **3**, 083602 (2015).

[26] M. Zeng, C. Fang, G. Chang, Y.-A. Chen, T. Hsieh, A. Bansil, H. Lin, and L. Fu, Topological semimetals and topological insulators in rare earth monopnictides, arXiv:1504.03492.

[27] R. Yu, H. Weng, Z. Fang, X. Dai, and X. Hu, Topological Nodal Line Semimetal and Dirac Semimetal State in Antiperovskite Cu_3PdN, Phys. Rev. Lett. **115**, 036807 (2015).

[28] G. Bian *et al.*, Topological nodal-line fermions in spin-orbit metal $PbTaSe_2$, Nat. Commun. **7**, 10556 (2016).

[29] G. Jotzu *et al.*, Experimental realisation of the topological Haldane model, Nature (London) **515**, 237 (2014).

[30] M. Atala, M. Aidelsburger, J. T. Barreiro, D. Abanin, T. Kitagawa, E. Demler, and I. Bloch, Direct measurement of the Zak phase in topological Bloch bands, Nat. Phys. **9**, 795 (2013).

[31] M. Lohse, C. Schweizer, O. Zilberberg, M. Aidelsburger, and I. Bloch, A Thouless quantum pump with ultracold bosonic atoms in an optical superlattice, Nat. Phys. **12**, 350 (2016).

[32] S. Nakajima, T. Tomita, S. Taie, T. Ichinose, H. Ozawa, L. Wang, M. Troyer, and Y. Takahashi, Topological Thouless pumping of ultracold fermions, Nat. Phys. **12**, 296 (2016).

[33] H.-I. Lu, M. Schemmer, L. M. Aycock, D. Genkina, S. Sugawa, and I. B. Spielman, Geometrical Pumping with a Bose-Einstein Condensate, Phys. Rev. Lett. **116**, 200402 (2016).

[34] L. Tarruell, D. Greif, T. Uehlinger, G. Jotzu, and T. Esslinger, Creating, moving and merging Dirac points with a Fermi gas in a tunable honeycomb lattice, Nature (London) **483**, 302 (2012).

[35] L. Huang, Z. Meng, P. Wang, P. Peng, S.-L. Zhang, L. Chen, D. Li, Q. Zhou, and J. Zhang, Experimental realization of a two-dimensional synthetic spin–orbit coupling in ultracold Fermi gases, Nat. Phys. **12**, 540 (2016).

[36] M. Gong, S. Tewari, and C. Zhang, BCS-BEC Crossover and Topological Phase Transition in 3D Spin-Orbit Coupled Degenerate Fermi Gases, Phys. Rev. Lett. **107**, 195303 (2011).

[37] K. Seo, L. Han, and C. A. R. Sá de Melo, Emergence of Majorana and Dirac particles in ultracold Fermions via Tunable Interactions, Spin-Orbit Effects, and Zeeman Fields, Phys. Rev. Lett. **109**, 105303 (2012).

[38] T. Das, Weyl semimetal and superconductor designed in an orbital-selective superlattice, Phys. Rev. B **88**, 035444 (2013).

[39] K. Seo, C. Zhang, and S. Tewari, Thermodynamic signatures for topological phase transitions to Majorana and Weyl superfluids in ultracold Fermi gases, Phys. Rev. A **87**, 063618 (2013).

[40] Y. Xu, R.-L. Chu, and C. Zhang, Anisotropic Weyl Fermions from the Quasiparticle Excitation Spectrum of a 3D Fulde-Ferrell Superfluid, Phys. Rev. Lett. **112**, 136402 (2014).

[41] H. Hu, L. Dong, Y. Cao, H. Pu, and X.-J. Liu, Gapless topological Fulde-Ferrell superfluidity induced by an in-plane Zeeman field, Phys. Rev. A **90**, 033624 (2014).

[42] B. Liu, X. Li, L. Yin, and W. V. Liu, Weyl Superfluidity in a Three-Dimensional Dipolar Fermi Gas, Phys. Rev. Lett. **114**, 045302 (2015).

[43] Y. Xu and C. Zhang, Topological Fulde-Ferrell superfluids of a spin-orbit coupled Fermi gas, Int. J. Mod. Phys. B **29**, 1530001 (2015).

[44] Y. Xu, F. Zhang, and C. Zhang, Structured Weyl Points in Spin-Orbit Coupled Fermionic Superfluids, Phys. Rev. Lett. **115**, 265304 (2015).

[45] P. Wang, Z. Q. Yu, Z. Fu, J. Miao, L. Huang, S. Chai, H. Zhai, and J. Zhang, Spin-Orbit Coupled Degenerate Fermi Gases, Phys. Rev. Lett. **109**, 095301 (2012).

[46] L. W. Cheuk, A. T. Sommer, Z. Hadzibabic, T. Yefsah, W. S. Bakr, and M. W. Zwierlein, Spin-Injection Spectroscopy of a Spin-Orbit Coupled Fermi Gas, Phys. Rev. Lett. **109**, 095302 (2012).

[47] T. Dubček, C. J. Kennedy, L. Lu, W. Ketterle, M. Soljačić, and Hrvoje Buljan, Weyl Points in Three-Dimensional Optical Lattices: Synthetic Magnetic Monopoles in Momentum Space, Phys. Rev. Lett. **114**, 225301 (2015).

[48] W.-Y. He, S. Zhang, and K. T. Law, The realization and dectection of Weyl semimetals in cold atomic systems, arXiv:1501.02348.

[49] Y.-J. Lin, K. Jiménez-García, and I. B. Spielman, Spin-orbit-coupled Bose-Einstein condensates, Nature (London) **471**, 83 (2011).

[50] J.-Y. Zhang, S. C. Ji, Z. Chen, L. Zhang, Z. D. Du, B. Yan, G. S. Pan, B. Zhao, Y. J. Deng, H. Zhai, S. Chen, and J. W. Pan, Collective Dipole Oscillations of a Spin-Orbit Coupled Bose-Einstein Condensate, Phys. Rev. Lett. **109**, 115301 (2012).

[51] C. Qu, C. Hamner, M. Gong, C. Zhang, and P. Engels, Observation of Zitterbewegung in a spin-orbit-coupled Bose-Einstein condensate, Phys. Rev. A **88**, 021604(R) (2013).

[52] R. A. Williams, M. C. Beeler, L. J. LeBlanc, K. Jiménez-García, and I. B. Spielman, Raman-Induced Interactions in a Single-Component Fermi Gas Near an s-Wave Feshbach Resonance, Phys. Rev. Lett. **111**, 095301 (2013).

[53] Z. Wu, L. Zhang, W. Sun, X.-T. Xu, B.-Z. Wang, S.-C. Ji, Y. Deng, S. Chen, X.-J. Liu, and J.-W. Pan, Realization of two-dimensional spin-orbit coupling for Bose-Einstein condensates, arXiv:1511.08170.

[54] This pseudo-time-reversal symmetry corresponds to the symmetry in the continous model defined by $\Pi^{-1}H\Pi = H$ with $\Pi = i\sigma_y\mathcal{K}\mathcal{P}$ and $\mathcal{P}^{-1}H\mathcal{P} = H(-x)$.

[55] X.-J. Liu, K. T. Law, and T. K. Ng, Realization of 2D Spin-Orbit Interaction and Exotic Topological Orders in Cold Atoms, Phys. Rev. Lett. **112**, 086401 (2014).

[56] S. Tewari and J. D. Sau, Topological Invariants for Spin-Orbit Coupled Superconductor Nanowires, Phys. Rev. Lett. **109**, 150408 (2012).

[57] S. Matsuura, P.-Y. Chang, A. P Schnyder, and S. Ryu, Protected boundary states in gapless topological phases, New J. Phys. **15**, 065001 (2013).

[58] D. Xiao, M.-C. Chang, and Q. Niu, Berry phase effects on electronic properties, Rev. Mod. Phys. **82**, 1959 (2010).

[59] F. Zhang, C. L. Kane, and E. J. Mele, Topological Mirror Superconductivity, Phys. Rev. Lett. **111**, 056403 (2013).

[60] S. A. Yang, H. Pan, and F. Zhang, Dirac and Weyl Superconductors in Three Dimensions, Phys. Rev. Lett. **113**, 046401 (2014).

[61] T. K. Koponen, T. Paananen, J.-P. Martikainen, M. R. Bakhtiari, and P. Törmä, FFLO state in 1-, 2-, and 3-dimensional optical lattices combined with a non-uniform background potential, New J. Phys. **10**, 045014 (2008).

[62] For SF1 and SF2 phases, the pseudo-time-reversal symmetry operators correspond to $\mathcal{T}_1 = \mathcal{T}$ and $\mathcal{T}_2 = s_z\mathcal{T}$, respectively. The inversion symmetry operators correspond to $\mathcal{I}_1 = \mathcal{I}$ and $\mathcal{I}_2 = s_z\mathcal{I}$, respectively.

[63] J. T. Stewart, J. P. Gaebler, and D. S. Jin, Using photoemission spectroscopy to probe a strongly interacting Fermi gas, Nature (London) **454**, 744 (2008).

[64] L. Duca, T. Li, M. Reitter, I. Bloch, M. Schleier-Smith, and U. Schneider, An Aharonov-Bohm interferometer for determining Bloch band topology, Science **347**, 288 (2015).